Direct observation of an 80 K colossal barocaloric temperature change in one cycle of pressure application and release

Shin-ichi Ohkoshi,[1,2,3]* Kazuo Isogai,[4] Koki Nishioka,[4] Kenta Imoto,[1,3] Yuuki Mineo,[1] Marie Yoshikiyo,[1,3] Asuka Namai,[1,3] Olaf Stefanczyk,[1,3] Hiroko Tokoro,[5] Eric Collet,[3,6] Ricardo G. T. Ramirez,[3,6] Elzbieta Trzop,[3,6] Marie-Hélène Lemée-Cailleau,[7] Thomas C. Hansen,[7] Kazuhiko Motodohi,[4] Takashi Momiki,[4] Tomoko Okimoto,[4] and Ryu Hatano[4]

[1] Department of Chemistry, School of Science, The University of Tokyo
7-3-1 Hongo, Bunkyo-ku, Tokyo 113-0033, Japan.
[2] Cryogenic Research Center, The University of Tokyo
2-11-16 Yayoi, Bunkyo-ku, Tokyo 113-0032, Japan.
[3] DYNACOM (Dynamical Control of Materials Laboratory) IRL 2015
CNRS, The University of Tokyo
7-3-1 Hongo, Bunkyo-ku, Tokyo 113-0033, Japan.
[4] Aisin Corporation, 2-1 Asahi-machi, Kariya, Aichi 448-8650, Japan.
[5] Department of Materials Science, Faculty of Pure and Applied Sciences, University of Tsukuba,
1-1-1 Tennodai, Tsukuba, Ibaraki, 305-8577, Japan.
[6] University of Rennes, CNRS, Institut de Physique de Rennes – UMR 6251, F-35000 Rennes, France.
[7] Institut Laue-Langevin – 71 avenue des Martyrs CS 20156, 38042 GRENOBLE Cedex 9 - France.

*To whom correspondence should be addressed
E-mail: ohkoshi@chem.s.u-tokyo.ac.jp

Contents: **Page**

§ 1. Movie Legends

Supplementary Movie 1. Direct measurement setup using a thermocouple and directly observed temperature change by pressure application and release. The initial part of the movie shows the experimental setup for the direct measurement of the temperature change upon pressure application and release. The view is zoomed in to the sample cell containing the **cyano-RbZnMnFe** pellet with a thermocouple. The next section shows an enlarged 360-degree view of the sample and thermocouple. Uniaxial pressure is applied in the vertical direction. The final part of the movie shows the experimentally observed time profile of the pressure (upper) and the sample temperature (lower) measured at 21 ºC.

Supplementary Movie 2. Thermal-fluid simulations of the temperature change upon pressure application and release. Shown on the left side is the simulation model around the sample pellet with a thermocouple. The first part of the movie shows the temperature distribution of the sample cross-section obtained from thermal-fluid simulations. Next, the time profile of the calculated temperature is shown. The calculation was performed under the condition that the heat release or absorption process occurs over several seconds, consistent with the experiment.

§ 2. Synthesis and characterization

Materials and characterization. The raw materials for the synthesis, manganese dichloride tetrahydrate (FUJIFILM Wako), zinc dichloride (FUJIFILM Wako), rubidium chloride (FUJIFILM Wako), and potassium hexacyanoferrate (FUJIFILM Wako) were used as purchased. Elemental analyses results were as follows: Calculated; Rb, 23.3; Mn, 13.8; Fe, 15.2; Zn, 1.4; C, 19.7; N, 22.9; H, 0.4 % : Found; Rb, 23.5; Mn, 13.8; Fe, 14.6; Zn, 1.5; C, 20.1; N, 23.2; H, 0.5 %, giving the formula of $RbMn_{0.92}Zn_{0.08}[Fe(CN)_6]\cdot 0.7H_2O$.

Crystal structures were determined from PXRD measurements and Rietveld analyses using the RIGAKU PDXL software. The structural information of the HT and LT phases are in CCDC-2479974 and CCDC-2479975, respectively, as crystallographic information files which are available from the Cambridge Crystallographic Data Centre: https://www.ccdc.cam.ac.uk/structures/. The density of the HT phase was obtained as 2.04 g cm^{-3} and that of the LT phase was 2.28 g cm^{-3}.

Magnetic measurements were performed using a superconducting quantum interference device magnetometer (SQUID). DSC measurements were conducted using a RIGAKU DSC8230 in nitrogen atmosphere with a temperature scan rate of 10 K min^{-1}. The powder-form sample of **cyano-RbZnMnFe** and the reference Al_2O_3 powder were measured in an aluminium pan. For the heat capacity measurements, a pellet-form sample was prepared; the relaxation method was used with a Quantum Design PPMS-6000 system. The modulation amplitude was set to 0.5% of the temperature at each measurement point.

§ 3. Thermogravimetric measurement

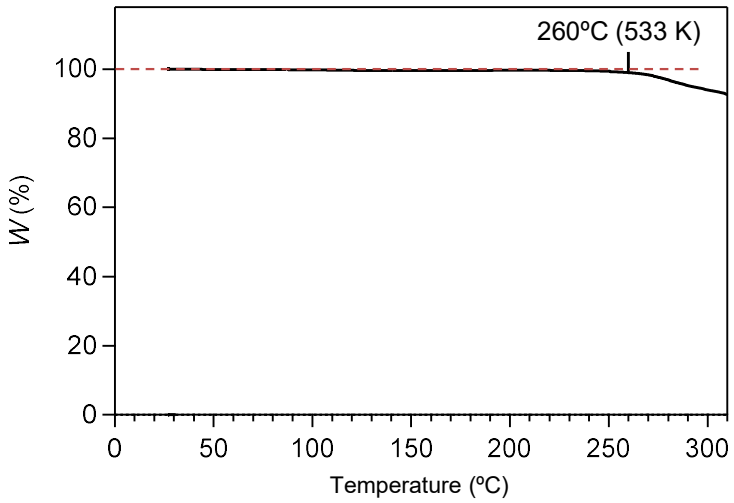

Figure S1. Thermogravimetric curve of **cyano-RbZnMnFe** measured under air flow. Mass loss at 260 ℃ corresponds to the decomposition of the CN groups.

§ 4. Crystal structure analysis and variable-temperature PXRD

(a)

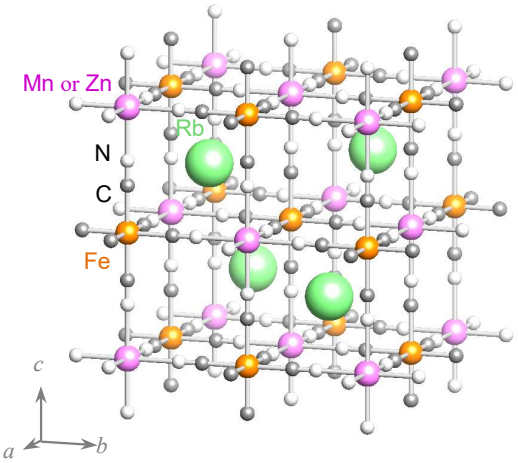

(b)

Formula	$C_6FeH_{1.4}Mn_{0.92}N_6O_{0.7}RbZn_{0.08}$
Formula weight	366.74
Crystal system	Cubic
Space group	$F\bar{4}3m$ (No. 216)
a (Å)	10.5488(2)
V (Å^3)	1173.84(3)
d_{cal} (g cm^{-3})	2.04
Z	4
R_{wp} (%)	4.63
S	1.63

Atomic pos.	*x*/*a*	*y*/*b*	*z*/*c*	Occ.	multiplicity
Rb	1/4	1/4	1/4	1	4
Fe	0	0	1/2	1	4
Zn	0	0	1/2	0.08	4
Mn	0	0	0	0.92	4
C	0	0	0.3118	1	24
N	0	0	0.2138	1	24
O1	1/4	1/4	3/4	0.044	4
O2	0.345	0.345	0.655	0.164	16

Figure S2. (a) Crystal structure of the HT phase of **cyano-RbZnMnFe** (cubic) at 300 K. Green, magenta, orange, grey, and light grey balls represent Rb, Zn/Mn, Fe, C, and N, respectively. O is omitted for clarity. (b) Structural details of the HT phase of **cyano-RbZnMnFe** (cubic) at 300 K obtained from the Rietveld analysis (CCDC-2479974).

(a)

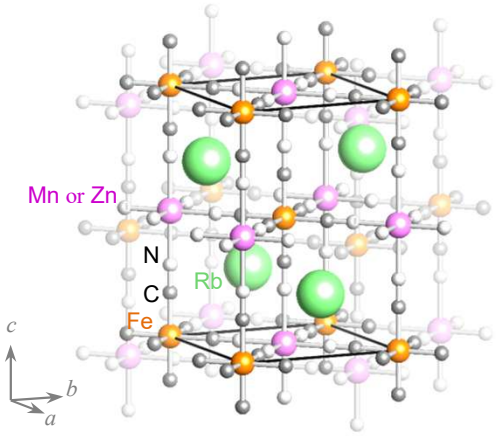

(b)

Formula	$C_6FeH_{1.4}Mn_{0.92}N_6O_{0.7}RbZn_{0.08}$
Formula weight	366.74
Crystal system	Tetragonal
Space group	$I\bar{4}m2$ (No. 119)
a (Å)	7.1042(3)
c (Å)	10.5319(5)
V (Å^3)	531.54(4)
d_{cal} (g cm^{-3})	2.28
Z	2
R_{wp} (%)	5.23
S	1.92

Atomic pos.	x/a	y/b	z/c	Occ.	multiplicity
Rb	0	1/2	1/4	1	2
Fe	0	0	0	1	2
Zn	0	0	1/2	0.08	2
Mn	0	0	1/2	0.92	2
C1	0	0	0.1738	1	4
N1	0	0	0.2847	1	4
C2	0.1882	0.1882	0	1	8
N2	0.3014	0.3014	0	1	8
O1	0	1/2	3/4	0.044	2
O2	0.306	0	0.153	0.164	8

Figure S3-1. (a) Crystal structure of the LT phase of **cyano-RbZnMnFe** (tetragonal) at 100 K. Green, magenta, orange, grey, and light grey balls represent Rb, Zn/Mn, Fe, C, and N, respectively. O is omitted for clarity. (b) Structural details of the LT phase of **cyano-RbMnZnFe** (tetragonal) at 100 K obtained from the Rietveld analysis (CCDC-2479975).

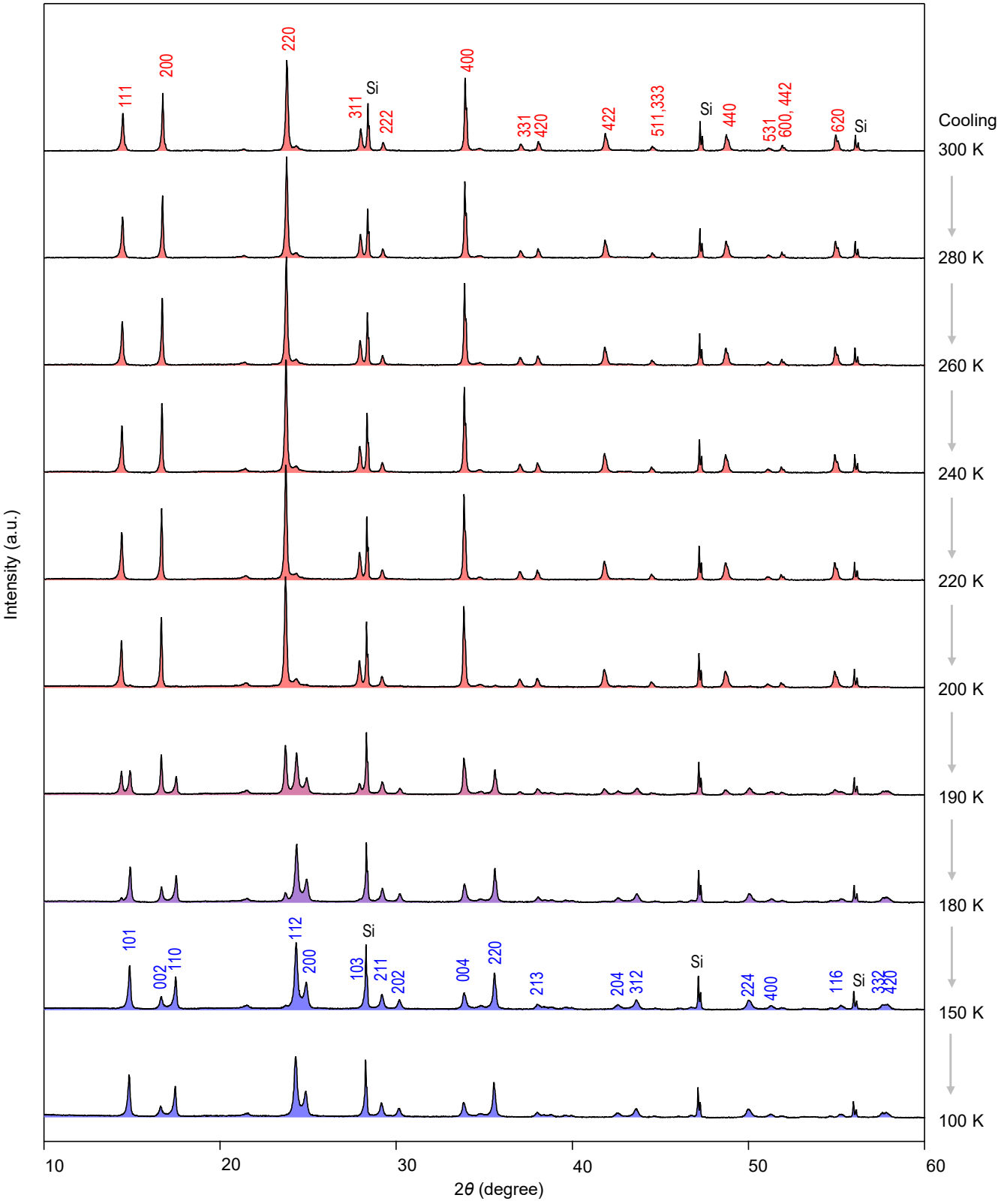

Figure S3-2. Cooling process of the temperature-dependent PXRD patterns. Red and blue peaks correspond to the HT and LT phases, respectively.

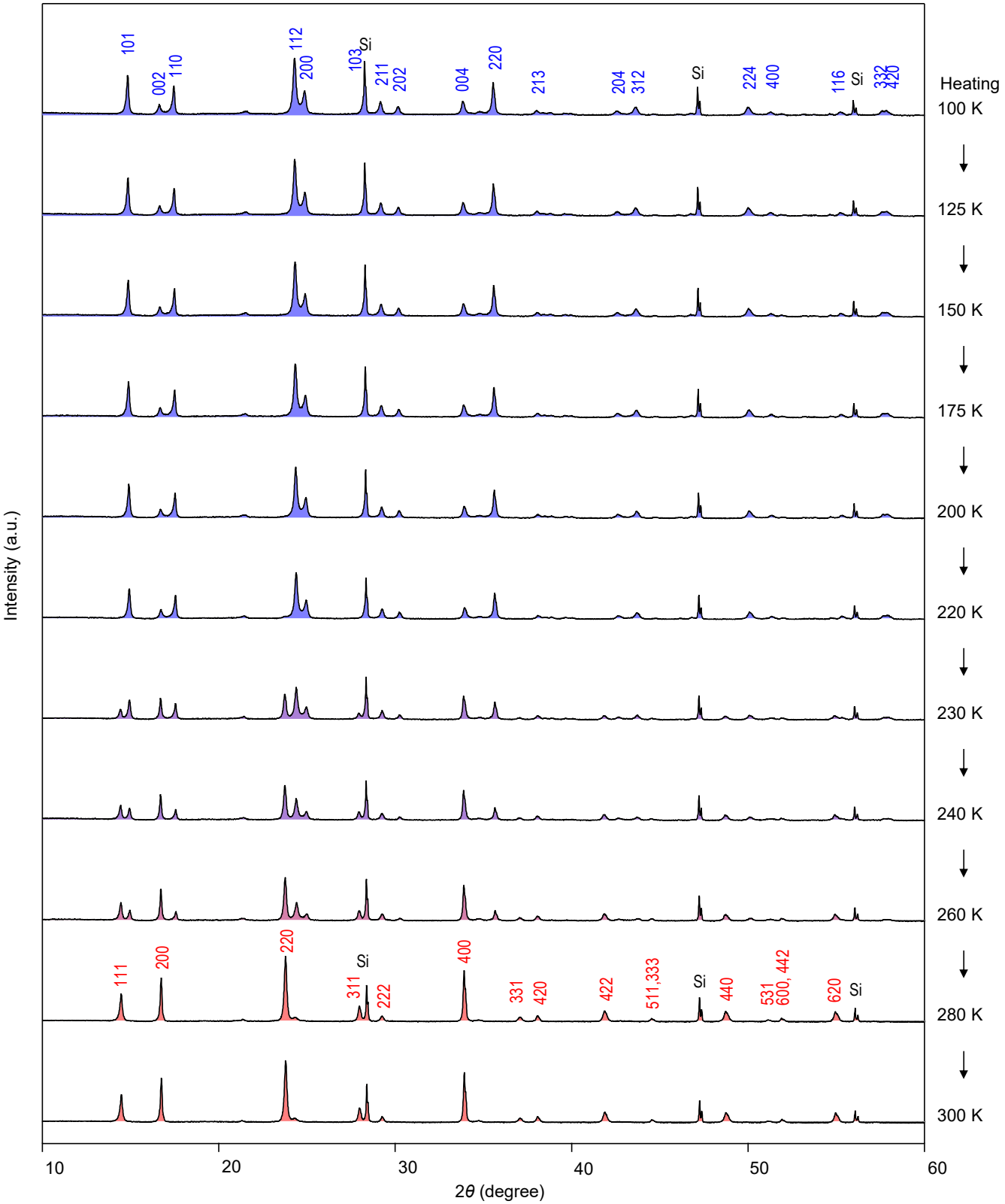

Figure S3-3. Heating process of the temperature-dependent PXRD patterns. Red and blue peaks correspond to the HT and LT phases, respectively.

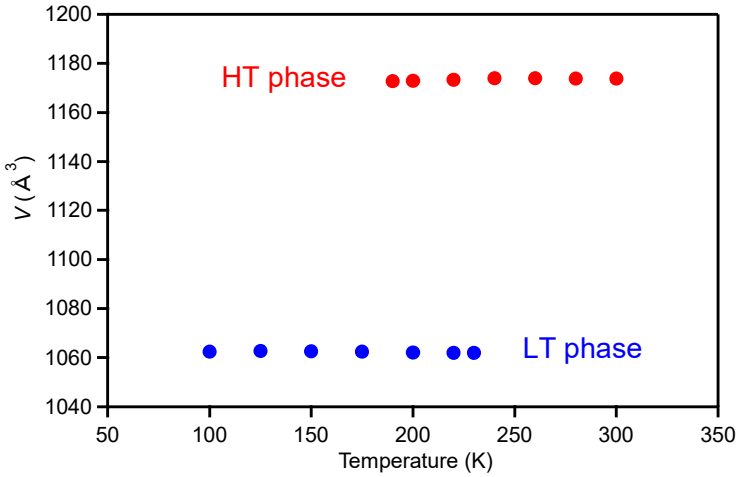

Figure S4. Temperature dependence of the lattice volumes at 0.1 MPa. Temperature dependence of the lattice volume V of the HT phase (red circles) and V' (= $2V$) of the LT phase (blue circles).

§ 5. Thermal hysteresis of magnetic susceptibility

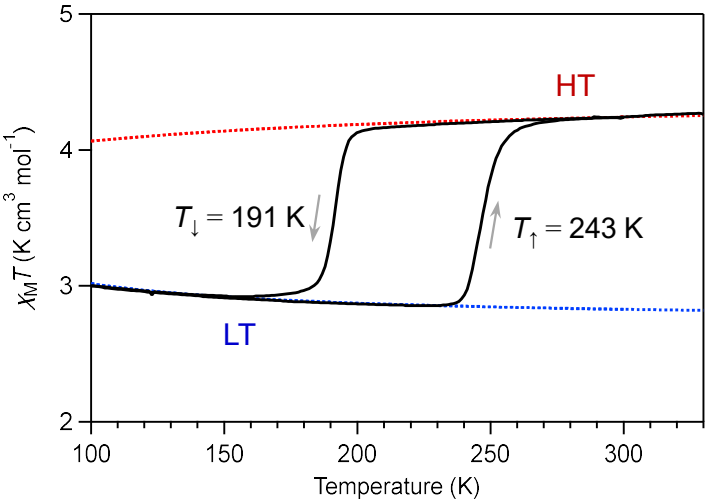

Figure S5. $\chi_M T$ versus temperature plot of **cyano-RbZnMnFe**, measured at ambient pressure under a 5000 Oe magnetic field with a sweeping rate of 1 K min^{-1}. Red and blue dotted lines indicate the fitted curves based on the MF theory for the HT and LT phases, respectively. The HT phase was fitted using a ferromagnetic superexchange interaction of 0.5 cm^{-1} and an antiferromagnetic superexchange interaction of −2.5 cm^{-1} between the Mn^{II} and Fe^{III} sites. The LT phase was fitted with a ferromagnetic superexchange interaction of +0.25 cm^{-1} between the Mn^{III} sites and an additional paramagnetic contribution from the Fe^{III} sites.

§ 6. Direct observation of temperature change by pressure application and release

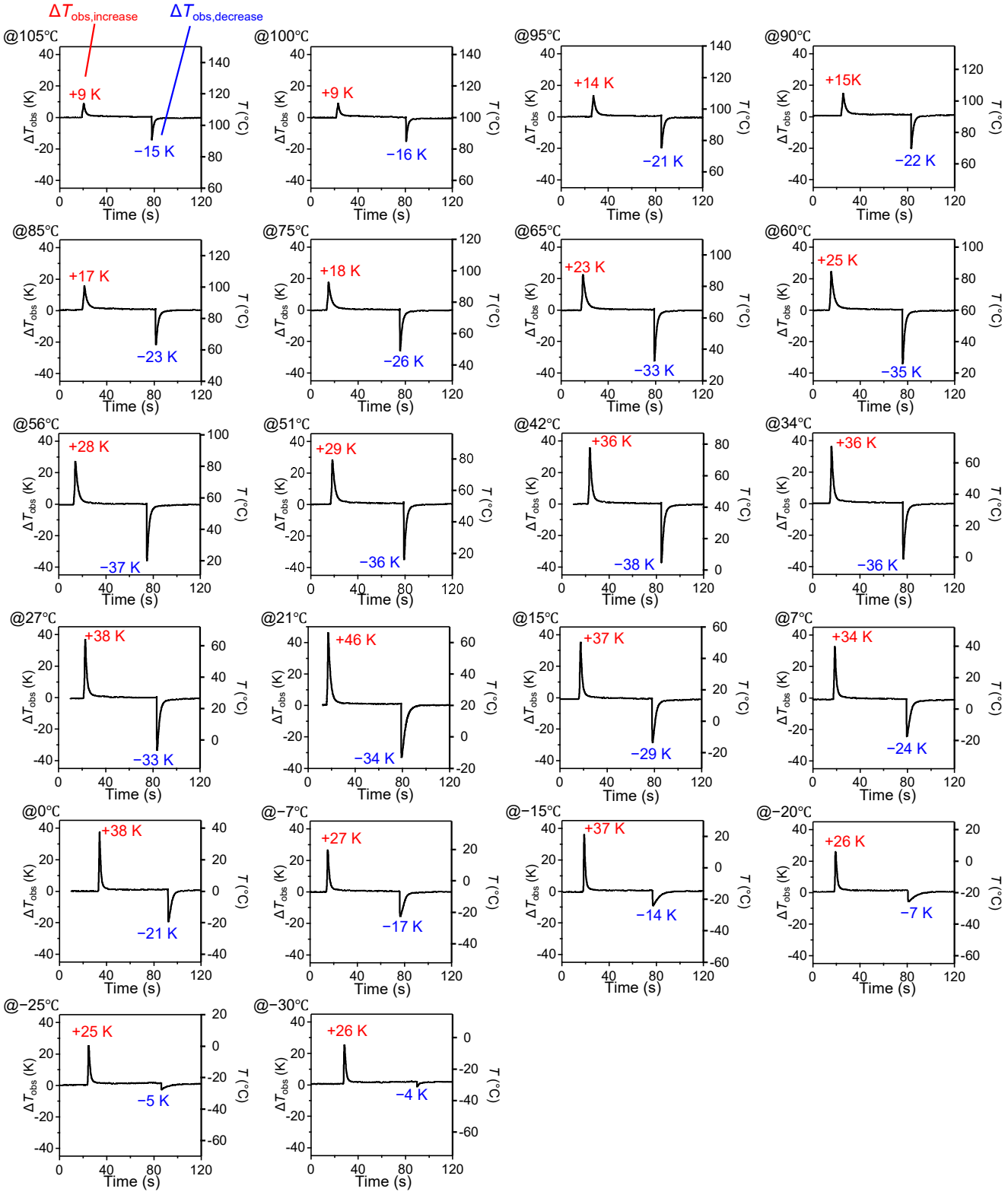

Figure S6-1. Temperature change upon pressure application (p_0= 0.1 MPa → p= 560 MPa) and release (p= 530 MPa → p_0) at various operation temperatures.

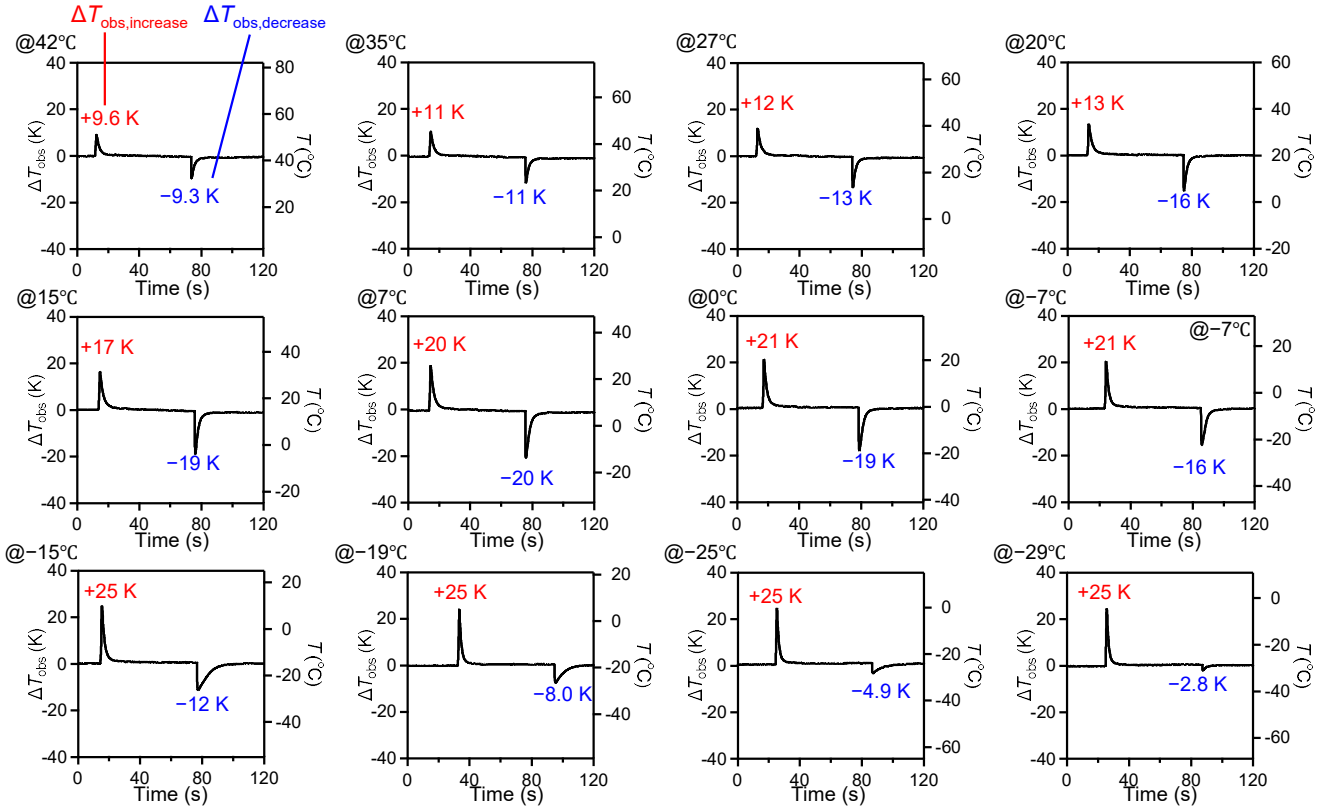

Figure S6-2. Temperature change upon pressure application (p_0= 0.1 MPa → p= 320 MPa) and release (p= 260 MPa → p_0) at various operation temperatures.

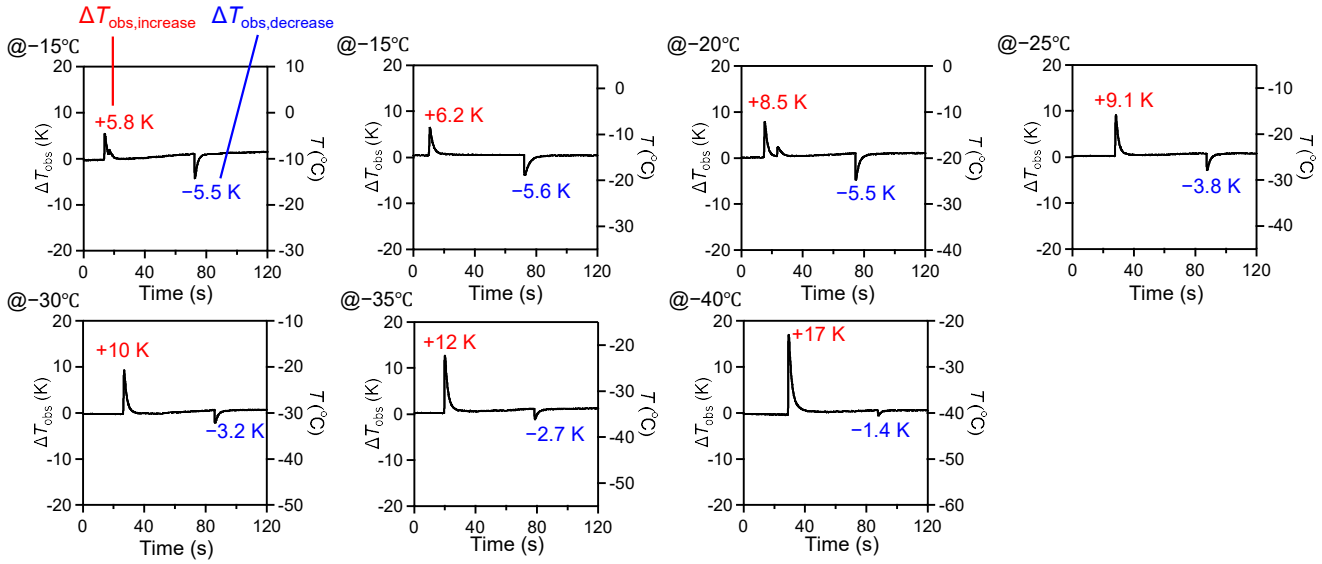

Figure S6-3. Temperature change upon pressure application (p_0= 0.1 MPa → p= 160 MPa) and release (p= 100 MPa → p_0) at various operation temperatures.

§ 7. Evaluation of the entropy curves

Using the relaxation method by PPMS, the heat capacity (C_p) versus temperature curve of the LT phase ($C_{p,LT}$) was obtained between 2 K and 235 K at ambient pressure p_0 (Fig. S7a). In the $C_{p,LT}$ curve, a magnetic anomaly due to the ferromagnetic phase transition occurs at the Curie temperature (T_C) of 10 K (Fig. S7a, inset). The entropy curve of the LT phase, $S_{LT}(T, p_0)$, was obtained by integrating $C_{p,LT}/T$ from 2 K to 235 K. Next, the exothermic peak from DSC between 185 K and 230 K was converted to entropy by integration (Fig. S7b), and then added to the $S_{LT}(T, p_0)$ curve from 185 K. Fig. S7c shows the C_p versus temperature curve of the HT phase ($C_{p,HT}$) obtained between 230 K and 260 K by PPMS, which was fitted using a heat capacity curve obtained from phonon mode calculations (Table S1)[24]. The fitted $C_{p,HT}$ curve was converted to entropy of the HT phase, $S_{HT}(T, p_0)$, by integrating $C_{p,HT}/T$. The $S_{LT}(T, p_0)$ and $S_{HT}(T, p_0)$ curves were extrapolated by integration of the fitted C_p curves based on phonon mode calculations. As for the entropy curves under pressure p, $S_{LT}(T, p)$ and $S_{HT}(T, p)$, the Maxwell relation and the expansion coefficients at 400 MPa obtained from neutron powder diffraction measurements were used (Fig. S7d), $\sigma \equiv (\partial S/\partial p)_T = -(\partial V/\partial T)_p$. The obtained σ values for the HT and LT phases are $\sigma = -2.5\times10^{-2}$ J K^{-1} kg^{-1} MPa^{-1} and $\sigma = -6.5\times10^{-3}$ J K^{-1} kg^{-1} MPa^{-1}, respectively, which are small compared to those for polymers or plastic crystals. This is reasonable because the present series of materials is reported to show zero or small thermal expansion. Figure S7e shows the entropy curves at 0.1 MPa and 560 MPa.

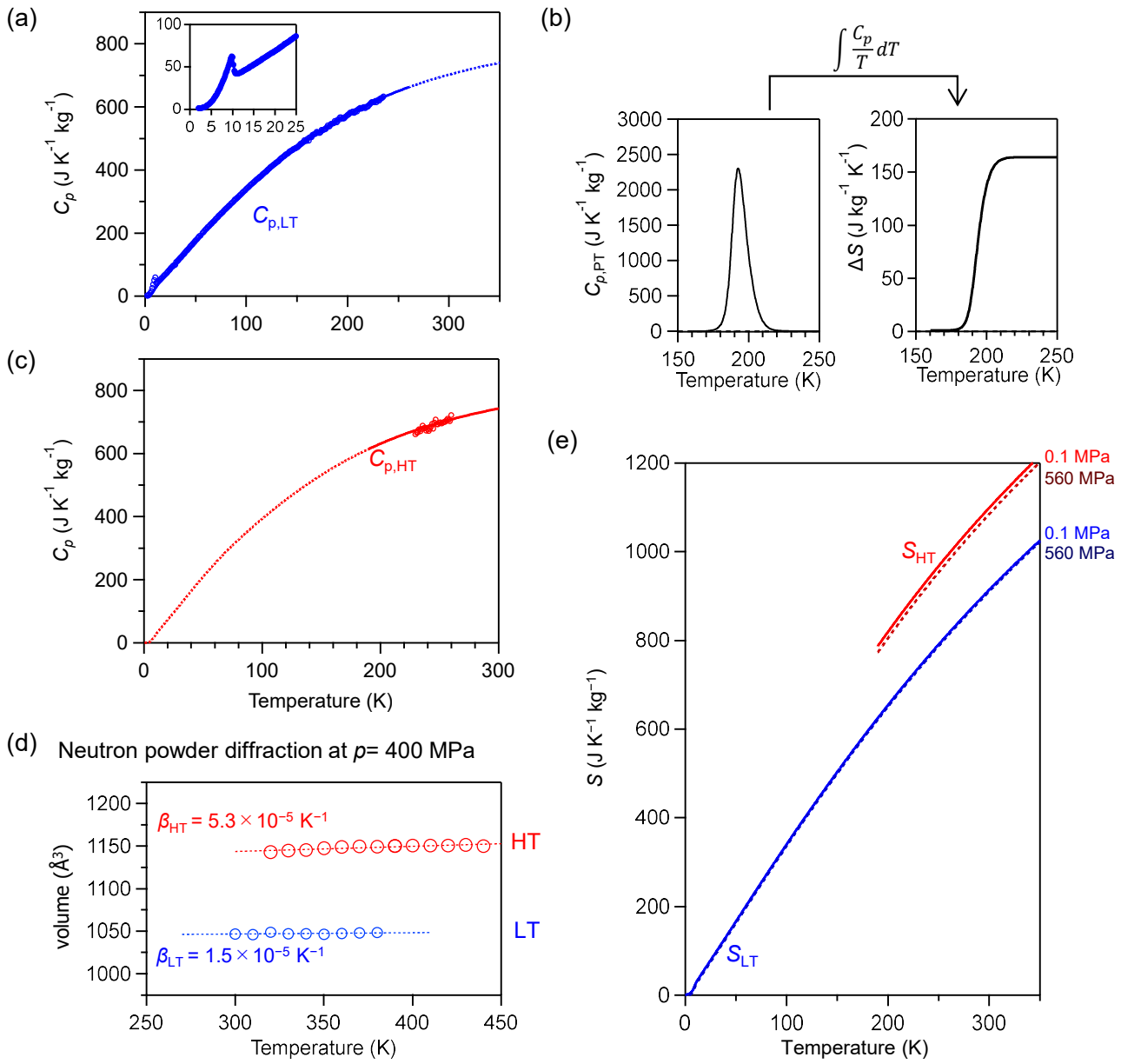

Figure S7. Thermodynamic properties of cyano-RbZnMnFe. (a) Heat capacity (C_p) for the LT phase obtained by PPMS. (b) Excess heat capacity due to the phase transition measured by DSC (left) and the converted ΔS curve (right). (c) C_p for the HT phase obtained by PPMS. Blue (a) and red (c) dotted lines are the fitted curves based on the heat capacity curves obtained from phonon mode calculations (Table S1). (d) Temperature dependence of the lattice volumes of HT phase (red circle) and LT phase (blue circle) obtained by neutron diffraction measurement at p= 400 MPa. (e) Pressure-dependent entropy versus T curves for the HT (red) and LT (blue) phases. Brown and navy dotted lines denote the entropy curves at 560 MPa (5.6 kbar) for the HT and LT phases, respectively.

Table S1. Heat capacity versus temperature data for the LT and HT phases of $RbMn[Fe(CN)_6]$ obtained by first-principles phonon mode calculations in our previous literature[24], which are used to fit the heat capacity measured by PPMS.

Temperature (K)	LT phase ($J\ K^{-1}\ kg^{-1}$)	HT phase ($J\ K^{-1}\ kg^{-1}$)	Temperature (K)	LT phase ($J\ K^{-1}\ kg^{-1}$)	HT phase ($J\ K^{-1}\ kg^{-1}$)
0	0	0	180	570.9	626.0
1	0.0003	0.0037	185	581.5	635.8
2	0.0377	0.0514	190	591.7	645.2
3	0.1819	0.3295	195	601.6	654.2
4	0.8304	1.407	200	611.2	662.9
5	2.690	3.726	205	620.4	671.3
10	25.59	27.23	210	629.3	679.3
15	49.28	52.71	215	637.9	687.0
20	70.30	76.60	220	646.2	694.4
25	90.19	100.2	225	654.2	701.5
30	109.4	124.0	230	661.9	708.3
35	128.3	148.2	235	669.4	714.8
40	146.9	172.6	240	676.6	721.1
45	165.5	196.6	245	683.5	727.1
50	184.0	220.1	250	690.2	732.9
55	202.3	242.8	255	696.7	738.5
60	220.4	264.6	260	702.9	743.9
65	238.2	285.5	265	708.9	749.0
70	255.8	305.5	270	714.7	754.0
75	273.0	324.8	275	720.3	758.8
80	290.0	343.5	280	725.7	763.4
85	306.8	361.6	285	730.9	767.8
90	323.2	379.2	290	736.0	772.1
95	339.4	396.4	295	740.8	776.2
100	355.4	413.2	296	741.8	777.0
105	371.1	429.5	300	745.6	780.2
110	386.6	445.5	310	754.6	787.7
115	401.8	461.1	320	763.0	794.7
120	416.8	476.3	330	770.9	801.3
125	431.4	491.1	340	778.3	807.5
130	445.8	505.5	350	785.3	813.3
135	459.8	519.4	360	792.0	818.7
140	473.6	533.0	370	798.2	823.9
145	487.0	546.1	380	804.2	828.8
150	500.0	558.8	390	809.8	833.4
155	512.7	571.0	400	815.2	837.9
160	525.1	582.8	425	827.7	848.1
165	537.1	594.2	450	838.9	857.3
170	548.7	605.2	475	849.1	865.8
175	560.0	615.8	500	858.6	873.6

§ 8. Barocaloric properties of representative solid materials

Table S2-1. Directly observed temperature change in one cycle of pressure application and release ($\Delta T_{obs,cycle}$) and the number of cycles for reported solid-state barocaloric materials around room temperature.

Materials	p (MPa)	$\Delta T_{obs,cycle}$ (K)	Number of cycles	References
cyano-RbZnMnFe	560	80	476	**This work**
cyano-RbMnFeCo	340	74	103	[1]
Acetoxy silicone rubber (ASR)	390	67	1	[2]
Ethylene propylene diene monomer (EPDM)	400	54.6	5	[3]
PDMS rubber	390	54	1	[4]
Vulcanized natural rubber (VNR)	390	43	1	[5]
Neopentylglycol (NPG)	231	37.5	10	[6]
Nitrile butadiene rubber (NBR)	390	31	1	[7]
$(C_{10}H_{21})_2NH_2Cl$	200	28.5	2	[8]
Polyurethane	218	25	1	[9]
1-Br-Adamantane/graphene composite	40	19.4	3	[10]
KPF_6	350	16.2	1	[11]
Ortho-carborane	300	16.2	4	[12]

[1] Ref. 24. S. Ohkoshi, et al. *Nat. Commun.* **14**, 8466 (2023) – read from the text on page 6.
[2] Ref. 47. W. Imamura, et al. *Chinese J. Polym. Sci.* **38**, 999–1005 (2020) – read from Fig. 2a.
[3] Ref. 48. Y. Li, et al., *J. Phys. Chem. B* **128**, 9297−9303 (2024) – read from the text on page 9298 and Fig. 4.
[4] Ref. 45. A. M. G. Carvalho, et al. *Eur. Polym. J.* **99**, 212–221 (2018) – read from Fig. 3a.
[5] Ref. 44. N. M. Bom, et al., *ACS Macro Lett.* **7**, 31–36 (2018). – read from Figs. S3.
[6] Ref. 18. K. Qian, et al. *Cell Rep. Phys. Sci.* **5**, 101981 (2024). – read from the text on page 7 and Fig. 3E.
[7] Ref. 46. E. O. Usuda, et al. *ACS Appl. Polym. Mater.* **1**, 1991−1997 (2019). – read from Fig. 3.
[8] Ref. 38. Y.-H. Gao, et al., *Nat. Commun.* **15**, 1838 (2024) – read from Figs. 4c, S9 and S10.
[9] Ref. 49. J. R. Bocca, et al. *Polym. Test.* **100**, 107251 (2021) – read from Fig. S6.
[10] Ref. 19. C. Bao, et al., *J. Mater. Sci. Technol.* **218**, 88−94 (2025) – read from Fig. 2d.
[11] Ref. 35. X. Zhao, et al., *Nat. Commun.* **16**, 7713 (2025) – read from Fig. S8.
[12] Ref. 50. K. Zhang, et al. *Adv. Funct. Mater.* **32**, 2112622 (2022) – read from Fig. 7a.

Table S2-2. Reversible adiabatic temperature change ($|\Delta T_{ad,rev}|$) of representative solid-state barocaloric materials around room temperature.

Materials	$\|\Delta T_{ad,rev}\|$ (K)	p (MPa)	References
cyano-RbMnFeCo	85	560	[1]
cyano-RbZnMnFe	83	560	**This work**
1-Br-adamantane	55	240	[2]
Neopentyl alcohol (NPA)	42	580	[3]
$Fe_3(bntrz)_6(tcnset)_6$	35	260	[4]
NH_4I	34	80	[5]
$LiCB_{11}H_{12}$	32	230	[6]
$(C_{10}H_{21}NH_3)_2MnCl_4$	32	250	[7]
Neopentyl glycol (NPG)	30	570	[8]
Polydimethylsiloxane	28.5	390	[9]
Neopentyl glycol (NPG)	24	590	[3]
$N(CH_3)_4[FeCl_4]$	21	90	[10]
Acetoxy silicone rubber	20.4	173	[11]
$(C_{10}H_{21})_2NH_2Cl$	19	100	[12]
AgI	18	250	[13]
$Fe(L)(NCS)_2$	16	100	[14]
Neopentyl alcohol (NPA)	16	260	[3]
$[Cp_2Fe][PF_6]$	16	100	[15]
$Fe(pap\text{-}5NO_2)_2$	14	200	[16]
$[Cp_2Co][PF_6]$	12	100	[15]
$(C_{10}H_{21}NH_3)_2MnCl_4$	12	100	[7]
$Fe(C_5H_5)(C_5H_4CHO)$	10	100	[17]
$LiCB_{11}H_{12}$	10	100	[6]
$(C_{10}H_{21}NH_3)_2MnCl_4$	7	50	[18]
$C_8H_{17}NH_3Cl$	6.2	100	[19]

[1] Ref. 24. S. Ohkoshi, et al. *Nat. Commun.* **14**, 8466 (2023) – read from the text on page 6.
[2] Ref. 14. A. Aznar, et al., *Appl. Mater. Today* **23**, 101023 (2021) – read from Fig. 6f.
[3] Ref. 13. A. Aznar, et al., *J. Mater. Chem. A* **8**, 639–647 (2020) – read from the text on page 645 for NPA, and Fig. 6e for NPG.
[4] Ref. 26. M. Romanini, et al., *Adv. Mater.* **33**, 2008076 (2021) – read from the text on page 6.
[5] Ref. 34. Q. Ren, et al. *Nat. Commun.* **13**, 2293 (2022) – read from Supplementary Fig. 3 and Fig. 4.
[6] Ref. 17. M. Zeng, et al., *Adv. Sci.* **11**, 2306488 (2024) – read from the text on page 5.
[7] Ref. 21. J. Li, et al. *Adv. Funct. Mater.* **31**, 2105154 (2021) – read from Fig. 5b and the text on page 6.
[8] Ref. 11. P. Lloveras, et al. *Nat. Commun.* **10**, 1803 (2019) – read from the text on page 5.
[9] Ref. 43. W. Imamura, et al. *J. Mater. Sci.* **57**, 311–323 (2022) – read from Table 2.
[10] Ref. 16. A. Salvatori, et al., *J. Mater. Chem. A* **11**, 12140–12150 (2023) – read from Fig. 9d and the text on page 8.
[11] Ref. 47. W. Imamura, et al. *Chinese J. Polym. Sci.* **38**, 999–1005 (2020) – read from the text on page 1003.
[12] Ref. 38. Y.-H. Gao, et al., *Nat. Commun.* **15**, 1838 (2024) – read from Fig. 2e.
[13] Ref. 33. A. Aznar, et al. *Nat. Commun.* **8**, 1851 (2017) – read from the text on page 3.
[14] Ref. 27. M. Seredyuk, et al., *Adv. Funct. Mater.* **34**, 2315487 (2024) – read from the text on page 9.
[15] Ref. 36. J. Garcia-Ben, et al., *J. Mater. Chem. A* **12**, 23751–23760 (2024) – read from the text on page 23756.
[16] Ref. 30. D. Gracia, et al., *J. Mater. Chem. A* **13**, 17944–17951 (2025) – read from the text on page 17949.
[17] Ref. 37. C. Bao, et al., *ACS Materials Lett.* **7**, 2451−2457 (2025) – read from Fig. 3f.
[18] Ref. 22. J. Seo, et al. *Nat. Commun.* **13**, 2536 (2022) – read from the text on page 6.
[19] Ref. 40. X. Wang, et al., *J. Mater. Chem. A* **13**, 1399–1406 (2025) – read from the text on page 1402.

Table S2-3. Temperature window (T_{span}) of representative solid-state barocaloric materials.

Materials	T_{span} (K)	p (MPa)	References
KPF_6	219	250	[1]
cyano-RbZnMnFe	152	560	**This work**
cyano-RbMnFeCo	142	560	[2]
Acetoxy silicone rubber	90	173	[3]
$N(CH_3)_4[FeCl_4]$)	82	220	[4]
1-Br-adamantane	75	240	[5]
$LiCB_{11}H_{12}$	70	230	[6]
$C_8H_{17}NH_3Cl$	65	100	[7]
$Fe_3(bntrz)_6(tcnset)_6$	65	260	[8]
NH_4I	51	80	[9]
$(C_{10}H_{21}NH_3)_2MnCl_4$	46	250	[10]
Neopentyl alcohol (NPA)	45	580	[11]
$LiCB_{11}H_{12}$	28	100	[6]
Neopentyl glycol (NPG)	28	570	[12]
AgI	27	250	[13]
$Fe(L)(NCS)_2$	27	100	[14]
$Fe(pap\text{-}5NO_2)_2$	26	200	[15]
$[Cp_2Co][PF_6]$	20	100	[16]
$[N_{2222}][TFSI]$	18	100	[17]
$[Cp_2Fe][PF_6]$	17	100	[16]
$Fe(C_5H_5)(C_5H_4CHO)$	16	100	[18]
$(C_{10}H_{21})_2NH_2Cl$	15	100	[19]
$(C_{10}H_{21}NH_3)_2MnCl_4$	12	50	[20]
$[C_{i3}mpyr][FSI]$	9	100	[17]
$[C_2mmor][FSI]$	8	100	[17]
$[C_{i3}mpyr][TFSI]$	7	50	[17]

[1] Ref. 35. X. Zhao, et al., *Nat. Commun.* **16**, 7713 (2025) – read from the text on page 2.
[2] Ref. 24. S. Ohkoshi, et al. *Nat. Commun.* **14**, 8466 (2023) – read from Fig. 3a.
[3] Ref. 47. W. Imamura, et al., *Chinese J. Polym. Sci.* **38**, 999–1005 (2020)– read from Fig. 3c.
[4] Ref. 16. A. Salvatori, et al., *J. Mater. Chem. A* **11**, 12140–12150 (2023) – read from Fig. 9c.
[5] Ref. 14. A. Aznar, et al., *Appl. Mater. Today* **23**, 101023 (2021) – read from Fig. 4c.
[6] Ref. 17. M. Zeng, et al., *Adv. Sci.* **11**, 2306488 (2024) – estimated from Fig. 3c.
[7] Ref. 40. X. Wang, et al., *J. Mater. Chem. A* **13**, 1399–1406 (2025) – read from the text on page 1403.
[8] Ref. 26. M. Romanini, et al., *Adv. Mater.* **33**, 2008076 (2021) – read from Fig. 6a.
[9] Ref. 34. Q. Ren, et al., *Nat. Commun.* **13**, 2293 (2022) – estimated from Supplementary Fig. 3h.
[10] Ref. 21. J. Li, et al., *Adv. Funct. Mater.* **31**, 2105154 (2021) – read from Fig. 5a.
[11] Ref. 13. A. Aznar, et al., *J. Mater. Chem. A* **8**, 639–647 (2020) – read from Fig. 4d.
[12] Ref. 11. P. Lloveras, et al., *Nat. Commun.* **10**, 1803 (2019) – read from Fig. 3c.
[13] Ref. 33. A. Aznar, et al., *Nat. Commun.* **8**, 1851 (2017) – read from Fig. 3c.
[14] Ref. 27. M. Seredyuk, et al., *Adv. Funct. Mater.* **34**, 2315487 (2024) – read from Fig. 7c.
[15] Ref. 30. D. Gracia, et al., *J. Mater. Chem. A* **13**, 17944–17951 (2025) – estimated from Fig.10a.
[16] Ref. 36. J. Garcia-Ben, et al., *J. Mater. Chem. A* **12**, 23751–23760 (2024) – read from the text on page 23756.
[17] Ref. 15. S. L. Piper, et al., *Science* **387**, 56–62 (2025) – estimated from Fig. 5.
[18] Ref. 19. C. Bao, et al., *ACS Materials Lett.* **7**, 2451−2457 (2025) – estimated from Fig. 3f.
[19] Ref. 38. Y.-H. Gao, et al., *Nat. Commun.* **15**, 1838 (2024) – estimated from Fig. 2d.
[20] Ref. 22. J. Seo, et al., *Nat. Commun.* **13**, 2536 (2022) – read from Fig. 5b.

Table S2-4. Refrigerant capacity for reversible cycles (RC_{rev}) of representative solid-state barocaloric materials.

Materials	RC_{rev} (J kg^{-1})	p (MPa)	References
cyano-RbZnMnFe	26600	560	**This work**
cyano-RbMnFeCo	26000	560	[1]
Neopentyl alcohol (NPA)	23000	580	[2]
Neopentyl alcohol (NPA)	17000	510	[2]
1-Br-adamantane	14500	240	[3]
Neopentyl glycol (NPG)	13000	590	[2]
$(C_{10}H_{21}NH_3)_2MnCl_4$	9000	250	[4]
$N(CH_3)_4[FeCl_4]$	8900	220	[5]
$LiCB_{11}H_{12}$	8500	230	[6]
$Fe_3(bntrz)_6(tcnset)_6$	5800	200	[7]
Pentaglycerol (PG)	5000	240	[2]
$Fe(C_5H_5)(C_5H_4CHO)$	4836	100	[8]
$(C_{10}H_{21})_2NH_2Cl$	3700	100	[9]
$(C_{10}H_{21}NH_3)_2MnCl_4$	3500	100	[4]
NH_4I	3200	80	[10]
$C_8H_{17}NH_3Cl$	3100	100	[11]
$LiCB_{11}H_{12}$	3100	100	[6]
Acetoxy silicone rubber	2600	173	[12]
$Fe(L)(NCS)_2$	2496	100	[13]
$[N_{2222}][TFSI]$	2087	100	[14]
Polydimethylsiloxane	1900	200	[15]
$Fe(C_5H_5)(C_5H_4CHO)$	1860	40	[8]
$(C_{10}H_{21}NH_3)_2MnCl_4$	1400	50	[16]
$[C_{i3}mpyr][FSI]$	910	100	[14]
$[Cp_2Fe][PF_6]$	800	100	[17]
$[Cp_2Co][PF_6]$	700	100	[17]
$Fe(pap\text{-}5NO_2)_2$	700	200	[18]
$[C_2mmor][FSI]$	607	100	[14]

[1] Ref. 24. S. Ohkoshi, et al. *Nat. Commun.* **14**, 8466 (2023) – read from the text on page 6.
[2] Ref. 13. A. Aznar, et al., *J. Mater. Chem. A* **8**, 639–647 (2020) – read from Fig. 6f.
[3] Ref. 14. A. Aznar, et al., *Appl. Mater. Today* **23**, 101023 (2021) – read from Fig. 6g.
[4] Ref. 21. J. Li, et al., *Adv. Funct. Mater.* **31**, 2105154 (2021) – read from Fig. 5c and the text on page 6.
[5] Ref. 16. A. Salvatori, et al., *J. Mater. Chem. A* **11**, 12140–12150 (2023) – estimated from Fig. 9c
[6] Ref. 17. M. Zeng, et al., *Adv. Sci.* **11**, 2306488 (2024) – estimated from Fig. 3c.
[7] Ref. 26. M. Romanini, et al., *Adv. Mater.* **33**, 2008076 (2021) – read from the text on page 6.
[8] Ref. 37. C. Bao, et al., *ACS Materials Lett.* **7**, 2451−2457 (2025) – read from the text on page 3452.
[9] Ref. 38. Y.-H. Gao, et al., *Nat. Commun.* **15**, 1838 (2024) – estimated from Fig. 2d.
[10] Ref. 34. Q. Ren, et al., *Nat. Commun.* **13**, 2293 (2022) – estimated from Supplementary Fig. 3h.
[11] Ref. 40. X. Wang, et al., *J. Mater. Chem. A* **13**, 1399–1406 (2025) – read from the text on page 1403.
[12] Ref. 47. W. Imamura, et al., *Chinese J. Polym. Sci.* **38**, 999–1005 (2020) – estimated from the product of normalized refrigerant capacity of ~15 kJ kg^{-1} GPa^{-1} and $|\Delta p|$ = 173 MPa given on page 1003.
[13] Ref. 27. M. Seredyuk, et al., *Adv. Funct. Mater.* **34**, 2315487 (2024) – read from the text on page 9.
[14] Ref. 15. S. L. Piper, et al., *Science* **387**, 56–62 (2025) – read from Table S19.
[15] Ref. 43. W. Imamura, et al., *J. Mater. Sci.* **57**, 311–323 (2022) – estimated from the product of normalized refrigerant capacity of 9.3 kJ kg^{-1} GPa^{-1} and $|\Delta p|$ = 200 MPa given in Table 4
[16] Ref. 22. J. Seo, et al., *Nat. Commun.* **13**, 2536 (2022) – read from Fig. 5c.
[17] Ref. 36. J. Garcia-Ben, et al., *J. Mater. Chem. A* **12**, 23751–23760 (2024) – estimated from Fig. 6.
[18] Ref. 30. D. Gracia, et al., *J. Mater. Chem. A* **13**, 17944–17951 (2025) – estimated from Fig. 10a.

§ 9. Reversible barocaloric effect

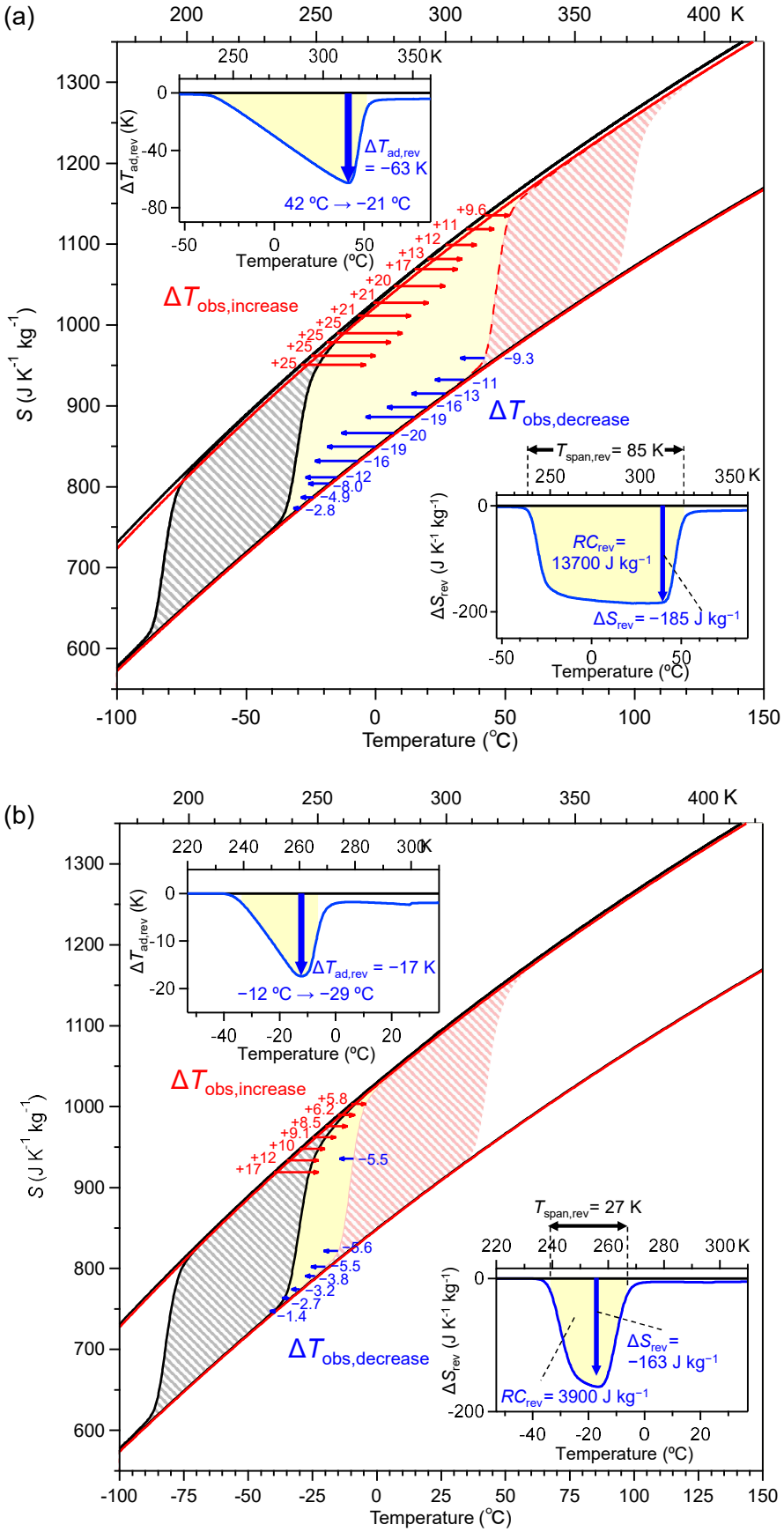

Figure S8. Entropy diagrams showing the entropy curves of the HT and LT phases at p_0 = 0.1 MPa (black line) and (a) p = 320 MPa and (b) 160 MPa (red line). Black and red shaded areas indicate the thermal hystereses at 0.1 MPa and 320 MPa or 160 MPa, respectively. The yellow areas show the reversible barocaloric region. Red and blue arrows show $\Delta T_{obs,increase}$ and $\Delta T_{obs,decrease}$, respectively. Insets show the temperature dependences of $\Delta T_{ad,rev}$ (upper left) and ΔS_{rev} (lower right).

§ 10. Origin of the entropy change

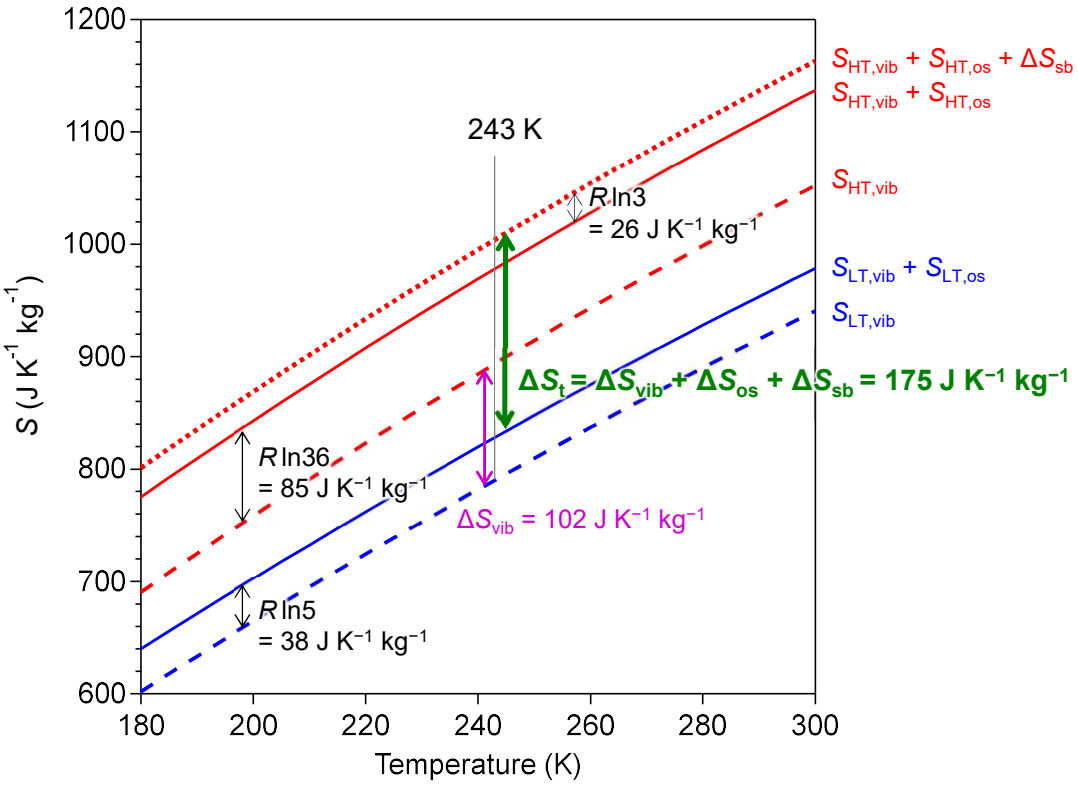

Figure S9. Temperature dependence of entropy for the HT (red) and LT (blue) phases obtained from PPMS and DSC measurements. Dashed lines indicate the vibrational entropy curves ($S_{HT,vib}$ and $S_{LT,vib}$). Solid lines include the contribution from orbital degeneracy and spin multiplicity ($S_{HT,os}$ and $S_{LT,os}$). Dotted red line additionally includes the entropy change from the symmetry breaking between cubic and tetragonal structures (ΔS_{sb}). Magenta arrow indicates the ΔS_{vib} value, and green arrow indicates the total ΔS_t value at the transition temperature of 243 K.

§ 11. Pressure dependence of transition temperature

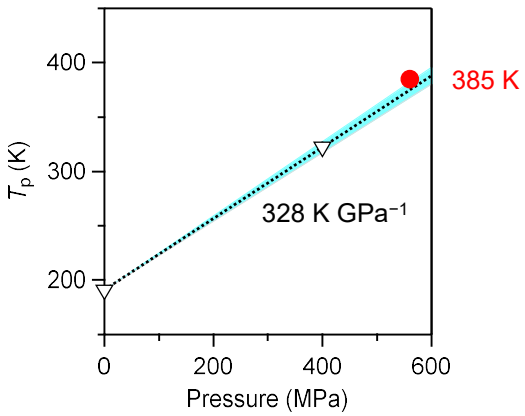

Figure S10. $T_{\downarrow}$ versus pressure plot. The plot at 0.1 MPa is from SQUID measurement, and that at 400 MPa is from high-pressure neutron powder diffraction measurement. The black dotted line is a fitted line, and blue color indicates the error.